Optics Letters

Photon-pair source working in a silicon-based detector wavelength range using tapered micro/nanofibers

Jin-Hun Kim,[1] Yong Sup Ihn,[1] Yoon-Ho Kim,[1,2] and Heedeuk Shin[1,3]

[1]Department of Physics, Pohang University of Science and Technology, Pohang 37673, South Korea
[2]e-mail: yoonho72@gmail.com
[3]e-mail: heedeukshin@postech.ac.kr

Received 13 November 2018; accepted 9 December 2018; posted 11 December 2018 (Doc. ID 351786); published 15 January 2019

The development of quantum photonic information technology demands high-quality photon sources. Here we demonstrate a low-noise and high-speed photon source generated by the spontaneous four-wave mixing process in a micro/nanofiber (MNF). The pair generation in a MNF is tailorable by controlling its diameter and designed for creating signal and idler photons in the silicon-based detector wavelength range, yielding high detection efficiency and coincidence count rate. This MNF photon source can be coupled to other fiber systems with negligible coupling loss and can be efficiently exploited as fiber-based quantum light sources for quantum information applications.

https://doi.org/10.1364/OL.44.000447

Robust, versatile, and bright photon sources are essential for the emerging field of quantum-enhanced technologies such as quantum communications [1,2], quantum teleportation [3–6], and quantum cryptography [7–9]. Over the past few decades, the spontaneous parametric down-conversion (SPDC)-based $\chi^{(2)}$ nonlinear birefringent crystals such as beta-barium borate crystals have been used for quantum optics experiments [10–15], and their high nonlinear coefficients and straightforward handling in experiments have made the crystals as the preferred photon sources for a long time. Despite these useful properties, as the SPDC scheme is mostly operational in the free space environment, it faces a challenge of high coupling loss when connecting the source to other fiber-based systems in practical applications, including long-distance communication system [16]. As an alternate candidate, the spontaneous four-wave mixing (SFWM)-based photon sources implemented in optical fibers have been extensively investigated, as the generated photons can be readily transported by connecting the photon sources directly to fiber-based systems with low-coupling loss [17–20].

Recently, an SFWM-based photon-pair source was demonstrated in a micro/nanofiber (MNF) [21]. The group-velocity-dispersion properties of MNF depend on the material dispersion, as well as the waveguide dispersion that is tailorable with the waveguide dimension [22]. Due to its small optical mode area, the photon-pair generation coefficient of MNF enhances significantly, and strong pair creation has been observed in a short length of MNF. The idler photons at 1310 nm were detected by an InGaAs-based single-photon detector (SPD) that has typically a low quantum efficiency of 10% and a low count rate due to the SPD saturation effect. Therefore, the maximum coincidence counts in Ref. [21] were about 6 kHz at the average pump power of 10 mW. Note that the use of silicon-based SPDs will yield a higher coincidence count rate.

In this Letter, we demonstrate the photon-pair generation by an SFWM process in a 12 cm long MNF with a 615 nm diameter fabricated out of a standard single-mode fiber (SM600, Fibercore). The numerical simulations are performed to determine the waveguide dimension for obtaining photon pairs at desired wavelengths. For the 725 nm pump beam and the 615 nm MNF diameter, the signal and idler photons are generated at 632 and 850 nm, respectively, which can be detected by silicon-based SPDs with high quantum efficiency. Raman noise photons are significantly suppressed due to the large wavelength detuning between pump and signal/idler photons. As a result, we achieve a high coincidence count rate of 100 kHz at the average pump power of 2 mW with a coincidence-to-accidental ratio (CAR) value of 18 and a high CAR value of more than 400 with two-fold coincidence counts around 130 Hz at the average pump power of 70 μW.

The SFWM process is a third-order optical nonlinear process yielding the creation of signal/idler photons and the annihilation of two pump photons simultaneously. This SFWM process occurs by satisfying the energy conservation and phase-matching condition given by [20]

$$\omega_s + \omega_i = 2\omega_p, \tag{1}$$

$$2\beta_p - \beta_s - \beta_i - 2\gamma P_p = 0, \tag{2}$$

$$\gamma = \frac{2\pi n_2}{\lambda_p A_{\text{eff}}}, \tag{3}$$

where $\beta_{j(j=p,s,i)}$ and $\omega_{j(j=p,s,i)}$ are the propagation constant and angular frequency of the pump, signal, and idler photons ($\omega_s > \omega_p > \omega_i$), respectively. The $2\gamma P_p$ term represents the contribution of the self-phase modulation, where γ is the nonlinear coefficient of the fiber, and P_p refers to the peak power of the pump laser. A_{eff} is the effective mode area of fiber, and $n_2 = 2 \times 10^{-20}$ m^2/W refers to the second-order nonlinear index of silica that is the primary material of optical fibers. Due to the small area (2×10^{-13} m^2), the nonlinear coefficient in the experiments is roughly 100 times larger than that of the standard SM600 fiber, and a large number of photon, therefore, can be generated in the relatively short length of 12 cm.

Both the material dispersion and the waveguide dispersion contribute to the optical dispersion of a waveguide, and the waveguide dimension strongly varies the waveguide dispersion. Therefore, the wavelengths of signal and idler photons in the MNF can be designed by changing the diameter of an MNF for the desired experimental environment. To determine an optimum diameter, we numerically calculated the effective refractive index and group- velocity-dispersion parameter of MNFs for various diameters by assuming a straightforward air-cladding structure [22], and then the phase-matching curves are obtained from the solution of Eqs. (1) and (2) for various MNF diameters as seen in Fig. 1(a). When the reasonable peak pump power (~1 W) is taken into account, the self-phase modulation term, $2\gamma P_p$, contributes the phase-matching condition that makes two different regions in the normal dispersion regime. In the wavelength region far from the pump, the phase-matched wavelengths are weakly power dependent. Near the pump wavelength indicated as the black dotted line in Fig. 1(a), on the other hand, the generated wavelengths are close to the pump wavelength, but the wavelength separation between the signal and idler photons increases as the pump power increases [23].

Using a pump laser at 725 nm and the MNF with the 615 nm diameter, the signal and the idler photons can be generated at 632 and 850 nm, and the quantum efficiencies of the silicon-based SPDs are 70% and 50%, respectively. Furthermore, background noise photons created by spontaneous Raman scattering (spRS) effects can be considerably reduced, even at the room temperature due to the large detuning from the pump wavelength [24,25]. The Raman spectrum was measured using an optical spectrum analyzer, a pump light at 725 nm, and a 5 m standard single-mode fiber (SM600) which is identical that of the MNFs fabricated in this Letter, having indistinguishable Raman spectra with tapered MNFs. Short-pass filters and long-pass filters are used in sequence to block the pump light while recording the spectrum using the optical spectrum analyzer as seen in Fig. 1(b). The purple and blue pillars and dashed line indicate the signal, idler, and pump wavelengths at 632, 850, and 725 nm, respectively. The results prove that the spRS photons are feeble at the signal and idler wavelengths, inducing low Raman noise photons.

A single-mode fiber (SM600, Fibercore) is heated and adiabatically pulled by two programmable fiber-pulling stages and a flame with oxygen/hydrogen mixture which is regulated by a mass flow controller [26,27]. The MNF diameter is measured by using the diffraction pattern analysis method [28]. As a result, the 12 cm long MNF was produced with the uniform diameter of 615 nm. Figure 2(a) shows the diameter profile of an MNF fabricated under similar tapering conditions. The mean value of the measured diameters over the 13 points on the uniform tapered waist is 616.8 nm with a standard

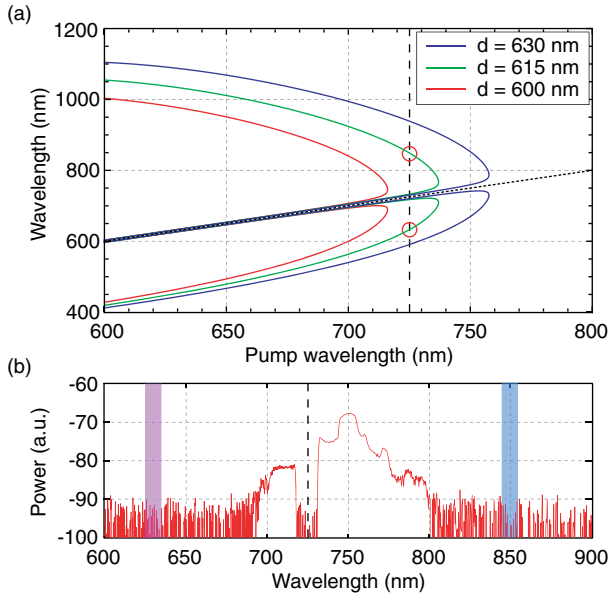

Fig. 1. (a) Phase-matching curves of the signal and idler for various MNF diameters, (d). Black dotted line represents the pump wavelength, and the vertical black dashed line indicates a pump wavelength of 725 nm used in this experiment. The vertical black dashed line meets the green phase-matching curve at 632 and 850 nm. (b) Measured Raman spectrum data. The vertical dashed line indicates the pump wavelength at 725 nm, and the purple and blue pillars represent the signal and idler photon wavelengths, respectively. The vertical axis is shown with log scale.

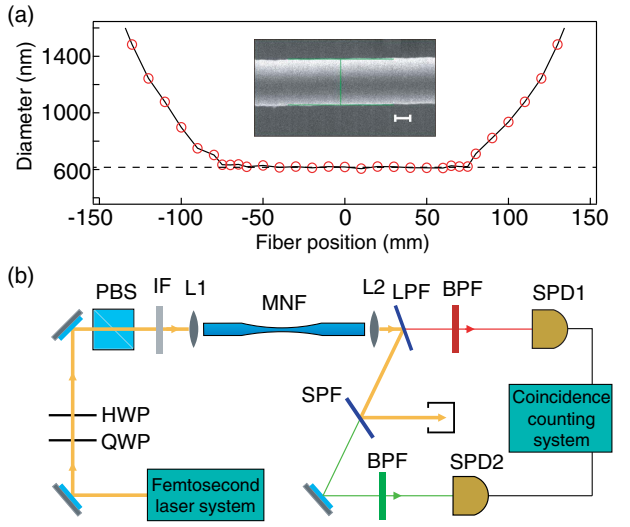

Fig. 2. (a) Profile of the measured MNF diameter. The uniform tapered waist is 12 cm long in length, and the waist diameter changes slowly to satisfy adiabatic condition. Inset, a SEM image of a section of the MNF fabricated under the identical conditions. The waist diameter from the SEM image is 618 nm. The scale bar is 200 nm. (b) Schematic optical setup. PBS, polarizing beam splitter; QWP, quarter-wave plate; HWP, half-wave plate; IF, interference filter; L1/L2, objective lens; LPF, long-pass filter; BPF, bandpass filter; SPF, short-pass filter; SPD1/SPD2; silicon-based SPD.

deviation of 17 nm. The inset in Fig. 2(a) shows the scanning electron microscope image of a section of a fabricated MNF.

The experimental setup is shown in Fig. 2(b). The pump source is a femtosecond mode-locked pulsed laser (MIRA, coherent) operating at a 725 nm-center wavelength with a repetition rate of 78 MHz. The average pump power is regulated by a quarter-wave plate, a half-wave plate, and a polarization beam splitter. Before coupling the pump light to the MNF, the pump beam passes through a spectral filter of 1 nm full width at half-maximum (FWHM) to remove unwanted photons, and the pulse duration after this filter is about 550 fs assuming the sech^2-shape pulses.

Since the generated signal and idler powers are much weaker than the pump power, the pump should be blocked for reliable detection of signal and idler photons. By using long-pass filters and short-pass filters, the pump, signal, and idler photons are split into three paths. Additional bandpass filters at 632 and 850 nm with a 10 nm FWHM help to further suppress the residual pump photons and the total isolation of the pump light is more than 190 dB. The signal and idler photons are then measured with silicon-based SPD1 and SPD2 (Excellitas), which have the quantum efficiency of about 70% and 50% at 632 and 850 nm, respectively. Their temporal correlation of the detection events is measured by the time-correlated single-photon counting device (quTAU, qutools).

Figures 3(a) and 3(b) show the individual single counting rate of the signal and idler photons against the pump power. The single count rates include the contributions of spRS noise photons and detector dark counts, as well as SFWM photons. The generation rate of the SFWM photon pairs is proportional to the square of the peak pump power, while that of spRS noise photons is linearly dependent on the peak pump power [20,24,29], and the dark counts are irrelevant to the pump power. To distinguish each contribution in the single counting rate, the quadratic polynomial models, $N_s = D_s + s_1 P_a + s_2 P_a^2$ and $N_i = D_i + i_1 P_a + i_2 P_a^2$, are fitted to the experimental data of the signal and idler ports, respectively. The fitting coefficients s_1 and i_1 are the strengths of spRS contributions, and s_2 and i_2 indicate the strengths of SFWM contributions in the signal and idler ports, respectively. D_s and D_i represent the dark counts of the signal and idler detectors having about 150 Hz.

As shown in Figs. 3(a) and 3(b), the solid blue squares represent the measured single count rates of the signal and idler ports, and the solid red lines are the fit curves. The extracted coefficients are $s_1 = 0.0097$ MHz/mW, $s_2 = 0.1385$ MHz/mW^2, $i_1 = 0.2046$ MHz/mW, and $i_2 = 0.0825$ MHz/mW^2. The spRS contribution in the idler port is higher than that of the signal port ($i_1 > s_1$), as the probability of the Stokes Raman scattering is higher than that of the anti-Stokes Raman scattering [24,29–31].

In both Figs. 3(a) and 3(b), individual contributions to the single counting rates from SFWM and spRS are displayed as the solid black and dashed black curves, respectively. The contribution from the dark counting is not shown in the figures, as it is negligible compared to the single counting rates. The SFWM contribution in the signal port is dominant due to the low Raman-based photon generation. The fitting coefficient s_2 of detected signal photons is larger than that i_2 of idler photons, indicating that the idler photons experience higher loss than signal photons. The plausible explanation for the different losses of the signal and idler ports is that the signal and idler photons experience different transmittance by the uncontrolled mode excitation in the adiabatic tapering regions [32]. The estimated transmittances of the MNF are 50% and 35% for the signal and idler photons, respectively. When we consider the quantum efficiencies of SPDs for the signal and idler wavelengths (70% and 50%), the overall efficiencies of the signal and idler ports are 31% and 20%, respectively.

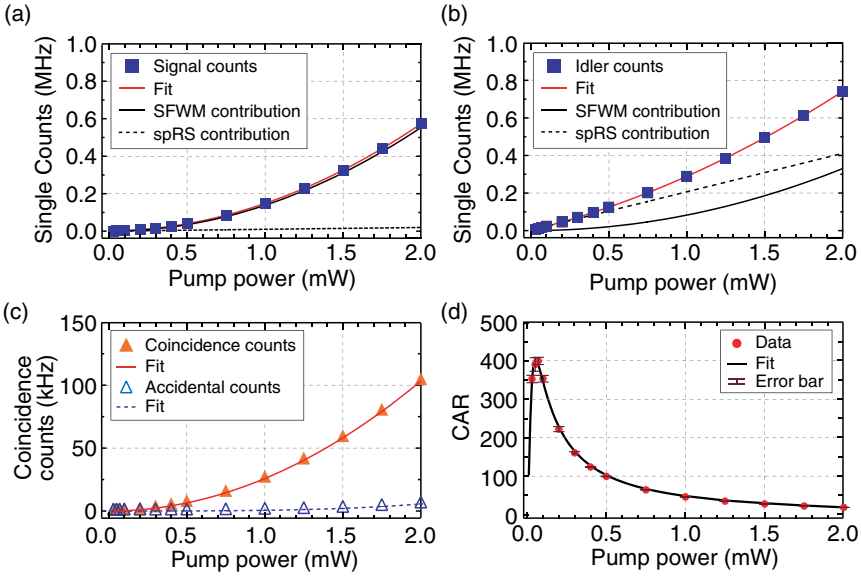

Fig. 3. Single-photon counting rates of (a) signal and (b) idler ports against the average pump power. The theoretical fits (red line) obtained using the quadratic polynomial models of N_s and N_i are shown as red curves atop the experimental data as blue squares. The dotted curves and dashed curves represent the spRS contribution and the SFWM contribution to the single count rates, respectively. (c) Experimentally measured two-fold coincidence counts and two-fold accidental counts. The superimposed solid black lines represent corresponding fits to each measured data. (d) Calculated CAR graph against the average pump power, and the solid black curves are fits to the measured data. The error bars of the data are within the size of data points in (a), (b), and (c), while the error bars in (d) are shown with the data points.

Figure 3(c) shows that the measured coincidence counts as the average pump power and the quadratic polynomial fits to data. The fitting result is dominantly proportional to the square of the pump power, indicating that the most of the coincidence events originate from the SFWM photon pairs [20]. The high coincidence count of about 100 kHz is achieved at a pump power of 2 mW (a peak pump power of 46.5 W) with silicon-based SPDs and high detection efficiency of the system (>20%). Compared with other SFWM-based quantum light sources, our system shows an unprecedented coincidence count and total detection efficiency [19,21,33–35]. The vertical error bar in Figs. 3(a)-3(c) represents the shot noise assuming a Poisson distribution of photons, but it is much smaller than the data markers.

In order to verify the quantum correlations between signal and idler photons generated in an MNF, the coincidence counts and accidental coincidence counts as seen in Fig. 3(c) are measured by recording the two-fold coincidence for the signal and idler photons generated by identical and different pulses, respectively. The two-fold coincidence counts at the same pump pulse include not only the coincidences between the correlated signal/idler photons, but also the accidental coincidences caused by photons from multiple pairs, the spRS noise photons, and the detector dark counts. The CARs are calculated from the measured data as seen in Fig. 3(d). The largest value of CAR is 405 at a pump power of 70 μW (a peak pump power of 1.6 W) with 127 Hz coincidence counts. In addition, a decent CAR value of 18 is achieved with about 100 kHz coincidence counts at a relatively high pump power of 2 mW (a peak pump power of 46.5 W). The vertical error bar in Fig. 3(d) is calculated from the shot noise of the data in Fig. 3(c). As the pump power increases, the CAR value gradually decreases due to the increase of accidental counting rates by multiple photon-pair generation and the combination of spRS photons and SFWM photons at a higher pump power.

In conclusion, we have demonstrated the generation of photon pairs by the SFWM process with high CAR values in a tapered 12 cm long MNF. The MNF photon-pair source is designed to work in the silicon-based detector wavelength range. The visible photon-pair generation has been investigated using crystals by SPDC causing significant development in quantum optics and quantum information technologies, but it has large loss when coupling to fiber systems. Recently, pair generations in the silicon-based detector wavelength range are reported in birefringent polarization maintaining fibers and photonic crystal fibers by SFWM [18,36,37]. In the case of birefrigent micro-structured fibers, small but non-zero optical coupling loss occurs when connecting to other optical fiber systems. The MNF scheme demonstrated in this Letter, however, creates photons in the silicon-based detector wavelength range and is able to be seamlessly spliced to other fiber-based quantum systems without polarization dependence. The MNF system can be a fiber-based, efficient, and wavelength-controllable quantum light source, and the experimental results prove that the MNF scheme with silicon-based SPDs can be efficiently exploited as efficient quantum light sources for quantum information applications.

Funding. National Research Foundation of Korea (NRF) (2016R1A2A1A05005202, 2016R1A4A1008978).

REFERENCES

1. N. Gisin and R. Thew, Nat. Photonics **1**, 165 (2007).
2. R. Ursin, F. Tiefenbacher, T. Schmitt-Manderbach, H. Weier, T. Scheidl, M. Lindenthal, B. Blauensteiner, T. Jennewein, J. Perdigues, P. Trojek, B. Ömer, M. Fürst, M. Meyenburg, J. Rarity, Z. Sodnik, C. Barbieri, H. Weinfurter, and A. Zeilinger, Nat. Phys. **3**, 481 (2007).
3. D. Bouwmeester, J.-W. Pan, K. Mattle, M. Eibl, H. Weinfurter, and A. Zeilinger, Nature **390**, 575 (1997).
4. Y.-H. Kim, S. P. Kulik, and Y. Shih, Phys. Rev. Lett. **86**, 1370 (2001).
5. I. Marcikic, H. De Riedmatten, W. Tittel, H. Zbinden, and N. Gisin, Nature **421**, 509 (2003).
6. X.-L. Wang, X.-D. Cai, Z.-E. Su, M.-C. Chen, D. Wu, L. Li, N.-L. Liu, C.-Y. Lu, and J.-W. Pan, Nature **518**, 516 (2015).
7. A. K. Ekert, Phys. Rev. Lett. **67**, 661 (1991).
8. C. H. Bennett, F. Bessette, G. Brassard, L. Salvail, and J. Smolin, J. Cryptol. **5**, 3 (1992).
9. C. H. Bennett, Phys. Rev. Lett. **68**, 3121 (1992).
10. P. G. Kwiat, K. Mattle, H. Weinfurter, A. Zeilinger, A. V. Sergienko, and Y. Shih, Phys. Rev. Lett. **75**, 4337 (1995).
11. P. G. Kwiat, E. Waks, A. G. White, I. Appelbaum, and P. H. Eberhard, Phys. Rev. A **60**, R773 (1999).
12. Y.-H. Kim, S. P. Kulik, M. V. Chekhova, W. P. Grice, and Y. Shih, Phys. Rev. A **67**, 010301 (2003).
13. T. Kim, M. Fiorentino, and F. N. C. Wong, Phys. Rev. A **73**, 012316 (2006).
14. R. Rangarajan, M. Goggin, and P. Kwiat, Opt. Express **17**, 18920 (2009).
15. Y.-C. Jeong, K.-H. Hong, and Y.-H. Kim, Opt. Express **24**, 1165 (2016).
16. A. Cuevas, G. Carvacho, G. Saavedra, J. Cariñe, W. A. T. Nogueira, M. Figueroa, A. Cabello, P. Mataloni, G. Lima, and G. B. Xavier, Nat. Commun. **4**, 2871 (2013).
17. J. Fan, A. Dogariu, and L. J. Wang, Opt. Lett. **30**, 1530 (2005).
18. J. Fan and A. Migdal, Opt. Lett. **15**, 2915 (2007).
19. H. Takesue and K. Inoue, Opt. Express **13**, 7832 (2005).
20. J. Chen, X. Li, and P. Kumar, Phys. Rev. A **72**, 033801 (2005).
21. L. Cui, X. Li, C. Guo, Y. H. Li, Z. Y. Xu, L. J. Wang, and W. Fang, Opt. Lett. **38**, 5063 (2013).
22. L. Tong, J. Lou, and E. Mazur, Opt. Express **12**, 1025 (2005).
23. A. Mcmillan, Y.-P. Huang, B. Bell, A. Clark, P. Kumar, and J. Rarity, *Single-Photon Generation and Detection*, A. Migdall, S. Polyakov, J. Fan, and J. Bienfang, eds., Vol. **45** of Experimental Methods in the Physical Sciences (Academic, 2013), p. 411.
24. X. Li, P. L. Voss, J. Chen, K. F. Lee, and P. Kumar, Opt. Express **13**, 2236 (2005).
25. D. J. Dougherty, F. X. Kärtner, H. A. Haus, and E. P. Ippen, Opt. Lett. **20**, 31 (1995).
26. T. A. Birksand and Y. W. Li, J. Lightwave Technol. **10**, 432 (1992).
27. G. Brambilla, V. Finazzi, and D. J. Richardson, Opt. Express **12**, 2258 (2004).
28. F. Warken and H. Giessen, Opt. Lett. **29**, 1727 (2004).
29. J. Auyeung and A. Yariv, IEEE J. Quantum Electron. **14**, 347 (1978).
30. L. Cui, C. Guo, X. Li, Y. H. Li, Z. Y. Xu, L. Wang, and W. Fang, in *CLEO: Science and Innovations* (Optical Society of America, 2014), paper JTh2A-18.
31. Y. Xu, L. Cui, X. Li, C. Guo, Y. Li, Z. Xu, L. Wang, and W. Fang, Chin. Phys. B **25**, 12 (2016).
32. A. Hartung, S. Brueckner, and H. Bartelt, Opt. Express **18**, 3754 (2010).
33. K. F. Lee, J. Chen, C. Liang, X. Li, P. L. Voss, and P. Kumar, Opt. Express **31**, 1905 (2006).
34. Q. Zhou, W. Zhang, J.-R. Cheng, Y.-D. Huang, and J. D. Peng, Opt. Express **18**, 17114 (2010).
35. Y. M. Sua, J. Malowicki, M. Hirano, and K. F. Lee, Opt. Express **38**, 73 (2013).
36. O. Alibart, J. Fulconis, G. K. L. Wong, S. G. Murdoch, W. J. Wadsworth, and J. G. Rarity, New J. Phys. **8**, 67 (2006).
37. B. J. Smith, P. Mahou, O. Cohen, J. S. Lundeen, and I. A. Walmsley, Opt. Express **17**, 23589 (2009).